

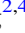






On the Nature of the Photospheric Horizontal Magnetic Field Increase in Major Solar Flares

Lijuan Liu^{1,2,3} , Zhenjun Zhou^{1,2} , Yuming Wang^{2,4} , Xudong Sun⁵ , and Guoqiang Wang⁶ ¹ Planetary Environmental and Astrobiological Research Laboratory (PEARL), School of Atmospheric Sciences, Sun Yat-sen University, Zhuhai, Guangdong, 519082, People's Republic of China; liulj8@mail.sysu.edu.cn² CAS Center for Excellence in Comparative Planetology, People's Republic of China³ Key Laboratory of Tropical Atmosphere-Ocean System, Sun Yat-sen University, Ministry of Education, Zhuhai, People's Republic of China⁴ CAS Key Laboratory of Geospace Environment, Department of Geophysics and Planetary Sciences, University of Science and Technology of China, Hefei, Anhui, 230026, People's Republic of China⁵ Institute for Astronomy, University of Hawai'i at Manoa, Pukalani, HI 96768, USA⁶ Institute of Space Science and Applied Technology, Harbin Institute of Technology, Shenzhen, People's Republic of China

Received 2022 June 1; revised 2022 July 21; accepted 2022 July 23; published 2022 August 4

Abstract

The rapid increase of the horizontal magnetic field (B_h) around the flaring polarity inversion line is the most prominent photospheric field change during flares. It is considered to be caused by the contraction of flare loops, the details behind which is still not fully understood. Here we investigate the B_h increase in 35 major flares using HMI high-cadence vector magnetograms. We find that the B_h increase is always accompanied by the increase of field inclination. It usually initiates near the flare ribbons, showing a step-like change in between the ribbons. In particular, its evolution in the early flare phase shows a close spatiotemporal correlation to flare ribbons. We further find that the B_h increase tends to have similar intensity in confined and eruptive flares but a larger spatial extent in eruptive flares in a statistical sense. Its intensity and timescale have inverse and positive correlations to the initial ribbon separations, respectively. The results altogether are well consistent with a recent proposed scenario that suggests that the reconnection-driven contraction of flare loops enhances the photospheric B_h according to the ideal induction equation, providing statistical evidence of the reconnection-driven origin for the B_h increase for the first time.

Unified Astronomy Thesaurus concepts: [Solar flares \(1496\)](#); [Solar activity \(1475\)](#); [Solar magnetic fields \(1503\)](#)

Supporting material: animations

1. Introduction

Solar flares are known as the process of sudden energy release caused by magnetic reconnection (Priest & Forbes 2002). They occur on timescales as short as minutes, during which the coronal magnetic field reorganizes rapidly, involving the eruption of the magnetic flux rope above and the formation of postflare loops below the reconnecting current sheet as suggested by the standard flare model (CHSKP model; see the review in Shibata & Magara 2011). The process, which occurs rapidly in tenuous corona, is not expected to exert considerable influence on the photosphere because the latter is much denser (Aulanier 2016). However, observations have revealed the counterintuitive fact that the photospheric magnetic field does undergo appreciable changes during flares (see review in Wang & Liu 2015; Toriumi & Wang 2019). The most prominent change is the abrupt, permanent increase of the horizontal magnetic field (B_h) around the flaring polarity inversion line (PIL), often accompanied by a B_h decrease in the peripheral sunspots (e.g., Wang et al. 2002; Sudol & Harvey 2005; Wang et al. 2012; Sun et al. 2017). Different from B_h , the vertical magnetic field (B_z) varies much less, without a clear pattern (Sun et al. 2017). Accompanied by the field changes, other photospheric signatures, such as the darkening of near-PIL penumbrae and weakening of peripheral

penumbrae (Liu et al. 2005; Wang et al. 2013), sunspot rotation (Wang et al. 2014), increase of field shear and inclination (Wang et al. 2012), etc., are also found.

The observations indicate an instant feedback from coronal eruptions to the photosphere, the nature of which is still not fully understood. The B_h increase around the flaring PIL, accompanied by the increase of field inclination, can be naturally interpreted by the “tilt” or contraction of flare loops above the core region. This is supported by the topological analysis of the coronal magnetic field during flares, which reveals that the field across the PIL collapses toward the photosphere after flares (Li et al. 2011; Liu et al. 2012; Sun et al. 2012). But what exactly causes the field collapse? The “magnetic implosion” conjecture is often cited as an explanation (Hudson 2000). It suggests that the coronal loops must contract to compensate for the energy decrease in the eruption region according to the rule of energy conservation. The sudden change in the corona may also excite an MHD wave that propagates downward and partially penetrates the photosphere to distort the field there (Fletcher & Hudson 2008; Hudson et al. 2008; Wheatland et al. 2018). Moreover, the photospheric field change is suggested to be useful for estimating the total Lorentz force change during eruptions and therefore useful for estimating the force impulse associated with the coronal mass ejection (CME) momentum (Fisher et al. 2012; Hudson et al. 2012).

The details of how the flare-loop contraction affects the photospheric field are not entirely clear. The implosion model mainly predicts the contraction of coronal loops, which does



Original content from this work may be used under the terms of the [Creative Commons Attribution 4.0 licence](#). Any further distribution of this work must maintain attribution to the author(s) and the title of the work, journal citation and DOI.

not seem to guarantee the field near the photosphere responds in a similar way (Sun et al. 2017). Moreover, although implosion is often related to the observed in-eruption contraction of nonerupting coronal loops (e.g., Gosain 2012; Simões et al. 2013; Wang et al. 2018), its relation to the observed flare-loop contraction (Ji et al. 2007; Liu et al. 2013) needs clarification. Besides, if the flare-loop contraction is just morphological, it may only affect B_h at the loop footpoints, forming disconnected, ribbon-like regions of B_h increase alongside the PIL, while the observed B_h increase occurs in the entire region covering the PIL. Further detailed explanation is needed. Recently, Barczynski et al. (2019) analyzed the 3D magnetic field in a generic MHD simulation of an eruptive flare to obtain more details of the above process. They concluded that the photospheric B_h increase resulted from the reconnection-driven contraction of flare loops, which can be well explained by the ideal induction equation ($\frac{\partial B_{x,y}}{\partial t} = -B_{x,y} \frac{\partial u_z}{\partial z}$; u_z is the vertical plasma velocity): the newly reconnected flare loops, which possess a strong line curvature and thus strong magnetic tension at their apex, may contract downward and drive the reconnection jet. The contraction process will brake when approaching the photosphere, resulting in negative $\frac{\partial u_z}{\partial z}$, which enhances the B_h under the loops through the induction equation. The work stressed the role of flare reconnection in enhancing B_h . Similar conclusions are drawn from a few observations, e.g., Liu et al. (2018) found a cotemporal and cospatial evolution trend between the B_h -increase region and flare ribbons; Wang & Liu (2021) discovered that the photospheric field inclination and running penumbral waves were affected by coronal reconnection. In addition to these case studies, extensive statistical research is needed.

To explore more details of photospheric field changes in flares, especially the role that flare reconnection plays, we perform a statistical research on the most prominent change— B_h increase—in 35 major flares using the high-cadence magnetograms provided by the Helioseismic and Magnetic Imager (HMI; Hoeksema et al. 2014; Sun et al. 2017) on board the Solar Dynamics Observatory (SDO). We mainly compared the characteristics of the B_h increase and flare ribbons.

2. Data

HMI measures the Stokes parameters at six wavelengths along the Fe I 6173 Å absorption line, based on which the photospheric vector magnetic field is derived by the Very Fast Inversion of the Stokes Vector algorithm (Hoeksema et al. 2014). The data has a plate scale of 0''5, with a cadence of 720 s for the regular product and of 90 s or 135 s for the high-cadence product. We select 35 major flares (all larger than M6.0 class; see Table 1), including 9 confined and 26 eruptive cases, from the first release of high-cadence data (Sun et al. 2017). For each flare, we create a set of cutout maps from full-disk magnetograms to track its source active region (AR). The cutout maps are reprojected from the native helioprojective–Cartesian coordinate to a local Cartesian cylindrical-equal-area coordinate for easier handling (Sun 2013). The formal uncertainty in the spectral line inversion is propagated as error in the data.

We check the flares' CME association by inspecting the SOHO LASCO CME catalog⁷ and analyze the flare ribbons' properties using the 1600 Å images provided by the Atmospheric Imaging Assembly (AIA; Lemen et al. 2012) on board SDO. The data has a plate scale of 0''6 and a cadence of 24 s. The saturation that sometimes appears in AIA images in major flares is corrected by replacing each problematic pixel with a value linearly interpolated from the pixel's two unsaturated values before and after the saturation period (Kazachenko et al. 2017).

3. Results

3.1. An Example of B_h Increase

3.1.1. Methods

We analyze the evolution of flare-related B_h increase case by case. An M6.6-class flare (SOL2015-06-22T17:39, case 33 in Table 1) is shown as an example (Figures 1 and 2). We first scrutinize the vector magnetograms and construct two masks of B_h increase, including a postflare mask used to pinpoint the final B_h -increase region (Figure 1(a)) and a spatiotemporal mask used to check the propagation of B_h increase (Figure 1(b)). The first mask consists of pixels where the postflare B_h increase exceeds 120 G (red patches enclosed by dark-green contours in Figure 1(a)). The pixels are identified from a B_h difference image constructed by subtracting a preflare B_h map from a postflare B_h map. The threshold for identifying the B_h increase, 120 G, is slightly higher than the HMI B_h uncertainty (Hoeksema et al. 2014). The second mask records the time when the B_h increase first reaches 120 G in each pixel. A similar method is performed on AIA 1600 Å images to obtain the spatiotemporal mask for flare ribbons (Figure 1(c)). We use a threshold several times larger than the median pixel value of all 1600 Å maps to identify the ribbon pixels (Kazachenko et al. 2017).

We further track the fronts of the B_h -increase region and flare ribbons to compare their propagation details. In each polarity, we select a representative point from the region front (either of the B_h -increase region or of flare ribbons), and track the point by measuring its distance to the PIL. The representative point (cyan squares in Figure 1(a)) is determined as the intersection between the region boundary and a slice perpendicular to the source PIL (S_p and S_n in Figure 1(a)). We choose the slices to be as close as possible to ribbons' initiation positions. The results are shown in Figure 2(a).

We also calculate a few parameters from the B_h -increase region to quantify its evolution, including the area, mean B_h (\bar{B}_h), total B_h (ΣB_h), mean shear angle (\bar{S}), mean inclination angle ($\bar{\theta}$; with respect to solar normal), and the proxy of the total photospheric excess magnetic energy density (ρ_{tot} ; Wang et al. 1996; Leka et al. 2003). The calculation details are shown in Table 2. \bar{B}_h quantifies the intensity, while ΣB_h and the area measure the extension of the B_h increase. $\bar{\theta}$ measures the field inclination. \bar{S} and ρ_{tot} quantify the deviation of the magnetic field from its potential state to some extent. If applicable, the temporal evolution of a parameter P is further fitted by a step-like function,

$$P(t) = a + bt + c \left\{ 1 + \frac{2}{\pi} \arctan[n(t - t_m)] \right\}, \quad (1)$$

⁷ https://cdaw.gsfc.nasa.gov/CME_list/index.html

Table 1
Flare Information and B_h -increase Characteristics

No.	Flare					Parameters								
	Class	Start	Location	AR	CME ^a	$\Delta \bar{B}_h$ Gauss	$\Delta \Sigma B_h$ $\times 10^{20}$ Mx	Area Mm ²	$\Delta \bar{\theta}$ degree	$\Delta \bar{\sigma}$ degree	$\Delta \rho_{\text{tot}}$ $\times 10^{22}$ erg cm ⁻¹	τ minutes	t_{start} minutes	IRS ^b Mm
1	M6.6	SOL2011-02-13T17:28	S20E05	11158	Y	334.5 \pm 98.2	3.4 \pm 1.0	101.6 \pm 3.9	3.0 \pm 2.0	1.0 \pm 2.1	2.04 \pm 0.02	0.6	16.2	3.4 \pm 0.2
2	X2.2	SOL2011-02-15T01:44	S20W12	11158	Y	294.2 \pm 97.3	7.8 \pm 2.6	252.5 \pm 11.4	6.0 \pm 2.3	3.5 \pm 2.5	4.66 \pm 0.04	1.4	12.4	4.1 \pm 0.0
3	X1.5	SOL2011-03-09T23:13	N08W11	11166	N	261.8 \pm 73.2	1.3 \pm 0.4	52.3 \pm 2.7	2.0 \pm 2.3	-4.7 \pm 2.4	0.25 \pm 0.02	2.8	6.4	5.8 \pm 0.3
4	M9.3	SOL2011-07-30T02:04	N14E35	11261	N	444.0 \pm 75.6	2.7 \pm 0.5	59.8 \pm 4.4	6.3 \pm 3.7	-8.2 \pm 4.2	1.18 \pm 0.03	3.2	5.8	4.3 \pm 0.2
5	M6.0	SOL2011-08-03T13:17	N16W30	11261	Y	331.1 \pm 179.9	6.9 \pm 3.8	206.2 \pm 11.8	5.7 \pm 3.3	2.2 \pm 4.1	1.88 \pm 0.02	1.1	45.1	14.0 \pm 0.8
6	M9.3	SOL2011-08-04T03:41	N16W38	11261	Y	263.7 \pm 85.1	6.7 \pm 2.4	258.5 \pm 14.7	4.0 \pm 3.8	1.3 \pm 4.5	3.64 \pm 0.03	5.7	11.9	6.0 \pm 0.3
7	X2.1	SOL2011-09-06T22:12	N14W18	11283	Y	382.0 \pm 84.6	6.6 \pm 1.6	173.9 \pm 8.7	6.3 \pm 3.3	2.1 \pm 4.1	3.41 \pm 0.03	3.8	10.7	6.5 \pm 0.8
8	X1.8	SOL2011-09-07T22:32	N14W31	11283	Y	324.1 \pm 98.9	6.4 \pm 2.2	185.0 \pm 14.4	4.9 \pm 4.8	-2.1 \pm 5.7	1.75 \pm 0.03	3.4	10.6	2.3 \pm 1.2
9	M8.7	SOL2012-01-23T03:38	N33W21	11402	Y	215.1 \pm 154.5	3.6 \pm 2.7	166.3 \pm 17.4	7.1 \pm 8.8	-7.8 \pm 9.7	1.06 \pm 0.03	5.3	42.9	16.1 \pm 2.1
10	X5.4	SOL2012-03-07T00:02	N18E31	11429	Y	278.4 \pm 168.1	20.5 \pm 13.2	720.6 \pm 51.8	9.9 \pm 3.5	2.4 \pm 3.7	11.02 \pm 0.08	5.7	18.0	3.4 \pm 1.0
11	X1.3	SOL2012-03-07T01:05	N15E26	11429	Y	186.3 \pm 142.0	3.4 \pm 2.8	176.3 \pm 18.2	5.3 \pm 6.0	2.7 \pm 6.6	1.28 \pm 0.05	0.3	11.8	24.6 \pm 0.9
12	M6.3	SOL2012-03-09T03:22	N15W03	11429	Y	224.2 \pm 210.5	6.2 \pm 5.9	275.5 \pm 18.6	3.2 \pm 4.3	-2.5 \pm 5.1	2.13 \pm 0.03	2.2	42.8	2.5 \pm 0.2
13	M8.4	SOL2012-03-10T17:15	N17W24	11429	Y	241.6 \pm 80.1	9.2 \pm 3.1	405.7 \pm 25.7	7.2 \pm 5.2	3.6 \pm 6.0	5.09 \pm 0.03	0.8	29.2	3.7 \pm 1.4
14	X1.4	SOL2012-07-12T15:37	S13W03	11520	Y	247.9 \pm 172.8	7.2 \pm 4.9	292.2 \pm 18.5	2.3 \pm 5.1	-1.0 \pm 8.8	1.62 \pm 0.02	17.2	84.4	61.8 \pm 0.0
15	M6.5	SOL2013-04-11T06:55	N09E13	11719	Y	167.8 \pm 228.7	0.6 \pm 0.8	36.8 \pm 3.6	3.8 \pm 4.6	2.6 \pm 7.1	0.12 \pm 0.01	0.2	40.1	10.3 \pm 1.2
16	M9.3	SOL2013-10-24T00:21	S09E10	11877	N	241.1 \pm 83.3	2.9 \pm 1.0	118.2 \pm 6.9	3.2 \pm 3.0	2.9 \pm 4.5	1.40 \pm 0.02	0.1	12.3	28.9 \pm 1.1
17	X3.3	SOL2013-11-05T22:07	S12E44	11890	Y	569.4 \pm 114.7	4.8 \pm 1.1	81.5 \pm 3.7	5.2 \pm 2.7	3.4 \pm 2.6	4.83 \pm 0.05	3.5	8.1	2.8 \pm 1.6
18	X1.1	SOL2013-11-08T04:20	S13E15	11890	Y	409.7 \pm 92.9	4.4 \pm 1.0	107.7 \pm 4.5	4.8 \pm 2.0	3.7 \pm 2.1	3.42 \pm 0.03	0.6	11.5	3.8 \pm 1.2
19	X1.1	SOL2013-11-10T05:08	S13W13	11890	Y	367.4 \pm 80.5	3.7 \pm 0.9	106.0 \pm 5.1	5.9 \pm 3.0	1.0 \pm 3.7	3.00 \pm 0.03	0.7	10.2	1.5 \pm 0.8
20	M9.9	SOL2014-01-01T18:40	S16W45	11936	Y	257.9 \pm 209.1	3.6 \pm 3.4	155.2 \pm 20.8	21.4 \pm 12.2	-4.4 \pm 13.1	-0.29 \pm 0.02	1.4	26.7	6.2 \pm 0.5
21	X1.2	SOL2014-01-07T18:04	S12W08	11944	Y	185.4 \pm 118.1	0.8 \pm 0.5	42.5 \pm 2.7	1.8 \pm 2.2	1.3 \pm 4.9	0.01 \pm 0.00	9.1	46.8	44.6 \pm 3.2
22	X1.0	SOL2014-03-29T17:35	N10W32	12017	Y	257.4 \pm 130.8	3.3 \pm 2.1	138.7 \pm 12.4	7.0 \pm 5.6	-3.0 \pm 6.7	0.19 \pm 0.02	3.2	18.0	2.5 \pm 0.4
23	X1.6	SOL2014-09-10T17:21	N11E05	12158	Y	208.5 \pm 173.2	8.0 \pm 7.0	381.7 \pm 22.4	3.4 \pm 2.6	0.1 \pm 4.1	1.88 \pm 0.02	1.2	49.3	24.0 \pm 1.1
24	M8.7	SOL2014-10-22T01:16	S13E21	12192	N	263.5 \pm 169.8	6.9 \pm 4.6	261.9 \pm 13.1	3.2 \pm 2.3	-2.6 \pm 2.6	0.71 \pm 0.02	5.4	53.0	51.3 \pm 1.9
25	X1.6	SOL2014-10-22T14:02	S14E13	12192	N	268.5 \pm 262.0	0.5 \pm 0.6	17.4 \pm 0.8	0.9 \pm 2.5	0.5 \pm 2.7	0.25 \pm 0.01	4.2	45.3	32.2 \pm 2.2
26	X3.1	SOL2014-10-24T21:07	S22W21	12192	N	144.5 \pm 87.3	3.6 \pm 2.2	250.1 \pm 21.4	5.4 \pm 4.5	-0.0 \pm 5.9	0.20 \pm 0.02	0.1	35.5	15.9 \pm 1.4
27	X2.0	SOL2014-10-26T10:04	S14W37	12192	N	175.5 \pm 131.0	1.4 \pm 0.8	58.2 \pm 10.5	25.4 \pm 9.8	-11.9 \pm 10.0	-0.26 \pm 0.01	24.4	33.7	28.5 \pm 0.3
28	X1.6	SOL2014-11-07T16:53	N17E40	12205	Y	375.8 \pm 263.3	11.7 \pm 8.4	309.3 \pm 19.7	6.9 \pm 3.2	0.4 \pm 3.4	4.75 \pm 0.07	3.6	35.0	6.0 \pm 2.7
29	M6.1	SOL2014-12-04T18:05	S20W31	12222	N	237.6 \pm 183.3	2.1 \pm 1.7	85.4 \pm 9.8	10.7 \pm 9.8	-6.9 \pm 11.1	0.05 \pm 0.01	1.1	36.9	11.7 \pm 0.4
30	M6.9	SOL2014-12-18T21:41	S11E10	12241	Y	243.2 \pm 162.3	9.1 \pm 6.1	374.0 \pm 16.5	4.2 \pm 2.8	1.3 \pm 3.6	2.80 \pm 0.03	0.1	38.6	6.0 \pm 0.2
31	X1.8	SOL2014-12-20T00:11	S19W29	12242	Y	267.4 \pm 134.4	14.8 \pm 7.6	547.7 \pm 36.4	4.8 \pm 3.7	1.8 \pm 4.5	7.40 \pm 0.06	3.1	24.4	3.1 \pm 0.0
32	X2.2	SOL2015-03-11T16:11	S17E22	12297	Y	326.2 \pm 144.8	6.6 \pm 2.8	207.0 \pm 9.8	3.2 \pm 2.2	3.2 \pm 2.2	5.49 \pm 0.04	3.0	17.7	13.9 \pm 1.4
33	M6.6	SOL2015-06-22T17:39	N13W06	12371	Y	235.1 \pm 55.8	10.4 \pm 2.5	443.6 \pm 15.6	4.5 \pm 1.8	2.1 \pm 2.2	7.67 \pm 0.04	11.6	24.9	4.6 \pm 0.0
34	X2.2	SOL2017-09-06T08:57	S08W32	12673	N	481.4 \pm 236.9	5.4 \pm 3.0	105.2 \pm 11.0	8.3 \pm 3.6	5.8 \pm 4.9	6.72 \pm 0.47	5.1	12.1	5.9 \pm 0.3
35	X9.3	SOL2017-09-06T11:53	S09W34	12673	Y	573.4 \pm 184.3	16.6 \pm 6.7	276.8 \pm 31.2	8.5 \pm 4.8	2.5 \pm 5.2	16.83 \pm 0.94	2.6	7.3	2.5 \pm 1.0

Notes.^a CME association of the flares. “Y” (“N”) refers to yes (no).^b IRS (initial ribbons separation) is averaged in the very early flare stage, with σ taken as the error. See calculation details for all parameters in Table 2.

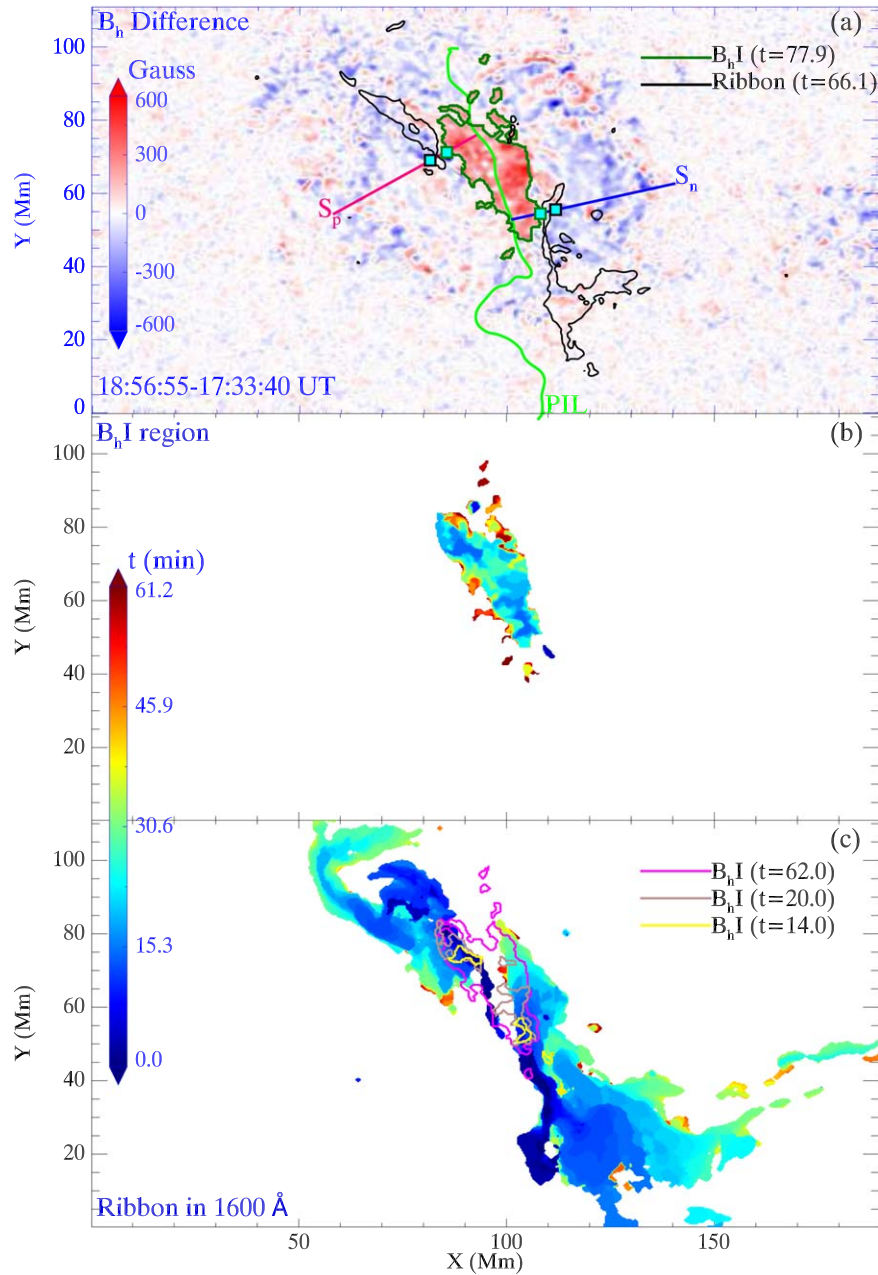


Figure 1. Evolution of B_h increase (abbreviated as “ B_h I” in figures) in case 33. (a) A postflare B_h difference image. The black-green contours outline the postflare mask of the B_h increase (pixel value ≥ 120 G); the black contours outline the flare ribbons at one moment for comparison. “ t ” (in minutes) indicates time after flare start (GOES start time). S_p and S_n are slices in positive and negative polarities used to determine the representative points of the region fronts (cyan squares). (b)–(c) Spatiotemporal evolution masks for the B_h increase and flare ribbons, color-coded by the time elapsed from flare start. Colored contours in (c) outline B_h -increase regions at different times. The associated animation lasts from 2017-09-06T17:38 to 2017-09-06T18:56, showing the B_h increase and ribbon evolution. Its frames have a similar layout to the figure.

(An animation of this figure is available.)

where a , b , c , n , and t_m are free parameters (Sudol & Harvey 2005; Sun et al. 2017). The term $a + bt$ indicates the linear evolution in addition to the step-like change; the parameter change is calculated by $\Delta P = 2c$; the change time-scale is given by $\tau = \pi/n$; t_m is the change midtime. We use IDL procedure `mpfit.pro`⁸ to perform the fitting. The parameters’ evolution, with errors propagated from the formal

uncertainty, is shown in Figures 2(b)–(g). The GOES 1–8 \AA flux is shown for comparison (blue curve in Figure 2(g)).

3.1.2. Features of the B_h Increase

The high-cadence data reveal the evolution details of the B_h increase. It is seen that the B_h increase starts from two kernels alongside the PIL (dark-blue patches in Figure 1(b) and yellow contours in Figure 1(c)), roughly coinciding with the flare ribbons’ initial positions. It then extends out (see Figure 1

⁸ <https://pages.physics.wisc.edu/~craig/idl/fitting.html>

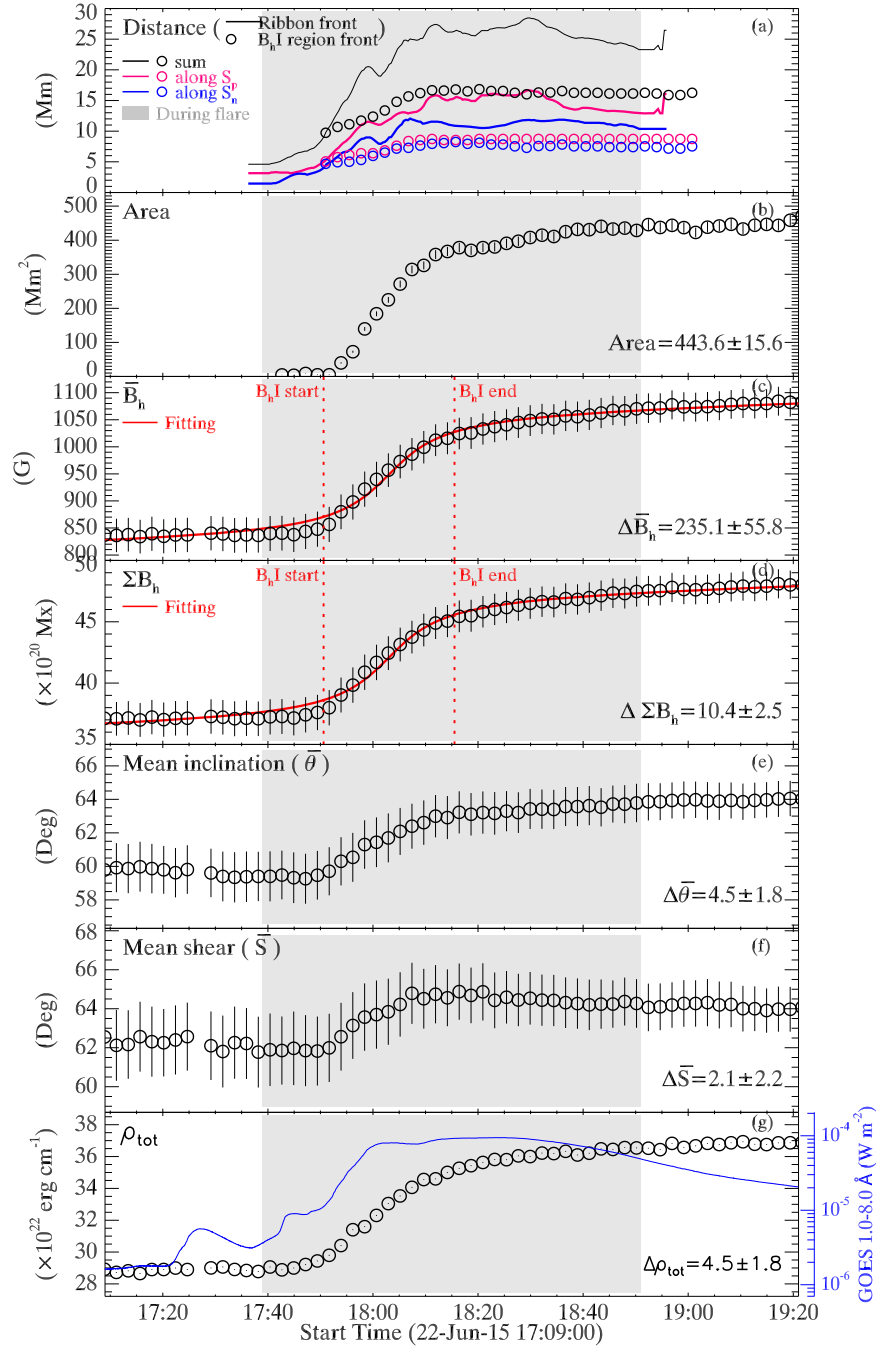


Figure 2. (a) Evolution of distances between the PIL and the fronts of the B_h -increase region (circles) and flare ribbons (lines) determined by the slices in Figure 1(a). Distances in both polarities (blue and red) and as sum (black) are shown. (b)–(g) Parameters quantifying the B_h increase. The vertical dashed lines in (c) and (d) mark the start and end times of the step-like changes obtained from the fitting. The associated animation lasts from 2017-09-06T17:38 to 2017-09-06T18:56, showing the parameters’ evolution accompanied by the B_h -increase region and ribbon evolution. Each frame contains parameter panels (similar as the figure) and two insets of the B_h -increase region and flare ribbons (similar as Figures 1(b)–(c)). The frame time is indicated by a vertical line in the parameter panels.

(An animation of this figure is available.)

associated movie), filling a whole region covering part PIL. The evolution of the region’s fronts (Figure 2(a)) further reveals that the B_h increase does follow the ribbon’s propagation in the early flare phase but remains almost still afterward while the ribbons propagate farther.

For the parameters quantifying the B_h increase (Figures 2(b)–(g)), the area reaches around 443.6 Mm^2 after the flare. \bar{B}_h and ΣB_h both show a step-like increase that can be fitted by Equation (1). The fitting reveals that \bar{B}_h begins to increase

minutes after the flare start (GOES start time) and lasts for 24.9 minutes. Its postflare change ($\Delta \bar{B}_h$) is 235.1 Gauss. The fitting of ΣB_h yields similar results. Its postflare change ($\Delta \Sigma B_h$) is $10.4 \times 10^{20} \text{ Mx}$. $\bar{\theta}$, \bar{s} , and ρ_{tot} also show a step-like change here, but their evolution in most other cases is too complicated to fit. To avoid the bias, we calculate the three parameters’ change here, as well as in other cases, by subtracting the preflare value from the postflare value instead of fitting (see details in Table 2). Here their changes ($\Delta \bar{\theta}$, $\Delta \bar{s}$, and $\Delta \rho_{\text{tot}}$) are

Table 2
Parameters Quantifying the B_h Increase and Flare Ribbons

Parameter ^a	Description	Calculation ^b	Unit	Type ^c	Change ^d
\bar{B}_h	Mean B_h	$\bar{B}_h = \frac{1}{n} \sum B_h$	Gauss	Intensive	$\Delta \bar{B}_h$
ΣB_h	Total B_h	$\Sigma B_h = \int B_h dA$	Mx	Extensive	$\Delta \Sigma B_h$
Area	Area	ΣdA	Mm ²	Extensive	Area
$\bar{\theta}$	Mean inclination angle	$\bar{\theta} = \frac{1}{n} \sum \arctan\left(\frac{B_x}{B_y}\right)$	Degree	Intensive	$\Delta \bar{\theta}$
\bar{S}	Mean shear angle	$\bar{S} = \frac{1}{n} \sum \arccos\left(\frac{\mathbf{B}_{pot} \cdot \mathbf{B}_{obs}}{ \mathbf{B}_{pot} \mathbf{B}_{obs} }\right)$	Degree	Intensive	$\Delta \bar{S}$
ρ_{tot}	Proxy for total photospheric magnetic free energy density	$\rho_{tot} = \frac{1}{8\pi} \sum (\mathbf{B}_{obs} - \mathbf{B}_{pot})^2 dA$	erg cm ⁻¹	Extensive	$\Delta \rho_{tot}$
τ	Timescale of B_h increase	Quoted from the step-like function (Equation (1)) fitting of \bar{B}_h evolution	Minutes		
t_{start}	Start time of B_h increase	As above	Minutes (since flare start)		
IRS	Initial ribbon separation	Ribbons separation averaged over a duration of 5 minutes before and 1 minute after the flare start	Mm		

Notes.

^a Area is calculated from the B_h -increase region identified at each moment. \bar{B}_h , ΣB_h , $\bar{\theta}$, \bar{S} , and ρ_{tot} are computed using the postflare B_h -increase mask.

^b Here n is the number of pixels of the B_h -increase region. B_{obs} is the observed field; B_{pot} is the potential field calculated by a Fourier transformation method (Alissandrakis 1981). The formulae for $\bar{\theta}$, \bar{S} , and ρ_{tot} are adapted from Bobra et al. (2014).

^c “Intensive”-type and “extensive”-type parameters measure the intensity and extension of the corresponding physical quantity, respectively.

^d Parameters change throughout the flares. $\Delta \bar{B}_h$ and $\Delta \Sigma B_h$ are quoted from the corresponding fittings. $\Delta \bar{S}$, $\Delta \bar{\theta}$, and $\Delta \rho_{tot}$ are calculated by subtracting the preflare value (averaged five minutes prior to the flare) from the postflare value (averaged five minutes after the flare). See relevant details in Section 3.1.

4.5, 2.1, and 4.5×10^{22} erg cm⁻¹, respectively, indicating the field in the B_h -increase region becomes more inclined and sheared after the flare.

3.2. Statistics of the B_h Increase

Using the above methods, we identify the B_h increase in all cases and perform statistical research. We found the postflare change of \bar{B}_h , $\Delta \bar{B}_h$, ranges from 144.5 G to 573.4 G in the sample, having a median of 263.5 G (Figure 3(a)). The change of ΣB_h , $\Delta \Sigma B_h$, has a median of 5.4×10^{20} Mx (Figure 3(b)). The area has a median of 176.3 Mm² (Figure 3(c)). The change of $\bar{\theta}$ ($\Delta \bar{\theta}$) shows an increase in all cases as well, having a median of 5.2 (Figure 3(d)). The change of \bar{S} ($\Delta \bar{S}$) shows an increase in about two-thirds (23) of the cases. Its median is 1.3 (Figure 3(e)). The change of ρ_{tot} ($\Delta \rho_{tot}$) displays an increase in 94% (33) of cases, having a median of 1.9×10^{22} erg cm⁻¹ (Figure 3(f)). The timescale of B_h increase, τ , ranges from 5.8 minutes to 84.4 minutes, having a median of 24.4 minutes (Figure 3(g)). The start time of the B_h increase, t_{start} , is generally small, having a median of 3.0 minutes (Figure 3(h)). τ and t_{start} are quoted from the \bar{B}_h evolution fitting. The results are consistent with previous observations that the field in the B_h -increase region becomes more inclined and sheared after flares.

When dividing the cases into confined and eruptive groups (Figure 3), the intensive parameter of the B_h increase, $\Delta \bar{B}_h$, shows very close medians in the two subsamples, suggesting a weak statistical difference. By contrast, the extensive parameters, $\Delta \Sigma B_h$ and area, show larger medians in eruptive flares. Similarly, $\Delta \bar{S}$ and $\Delta \rho_{tot}$, also have larger medians in eruptive flares. $\Delta \bar{\theta}$ and t_{start} show no significant statistical difference in the two subsamples. Only τ has a larger median in confined flares. These suggest that B_h increase occurs in either confined

or eruptive flares, having similar intensity in both kinds but larger spatial extent in eruptive flares.

We also compare the propagation of the B_h -increase region and flare ribbons in all cases by tracking their fronts (Figure 4). It is seen that the B_h increase always appears after the flare ribbons appear, with 60% (21) of cases initiating quite close to the ribbons (with a separation ≤ 5 Mm). The region then widens, manifested as the front progressing, in the early phase of most flares. Only in seven cases (e.g., case 4) does the region front barely move after appearance (progressing ≤ 2 Mm). Throughout the flare, the B_h -increase region evolves in between the straight parts of the flare ribbons and stops growing before the ribbons stop progressing, as suggested by the increasing distance between their fronts. The results indicate that in general, B_h increase and flare ribbons have close spatiotemporal correlations in the early flare phase.

The summed value of the distances from the ribbon’s fronts to the PIL in both positive and negative polarities (green curves in Figure 4) represents the separation between flare ribbons. Because the straight parts of the flare ribbons highlight the footpoints of the flare loops as suggested in the 3D extension of the standard flare model (Aulanier et al. 2012; Janvier et al. 2013), the ribbons’ separation can indicate the height of the loops if a nearly semicircular shape of the loops is considered (Fletcher & Hudson 2008; Thalmann et al. 2015; Kusano et al. 2020). Therefore, the ribbons’ separation obtained in the very early flare stage, defined as the initial ribbon separation (IRS) here (see calculation details in Table 2), indicates the height where early flare loops are formed, i.e., where flare reconnection initiates. We then check the correlation between the IRS and B_h -increase parameters. Interestingly, we find a rough inverse correlation between $\Delta \bar{B}_h$ and IRS (Figure 5(a)). Their relation can be roughly fitted by an exponentially decaying function in the form of

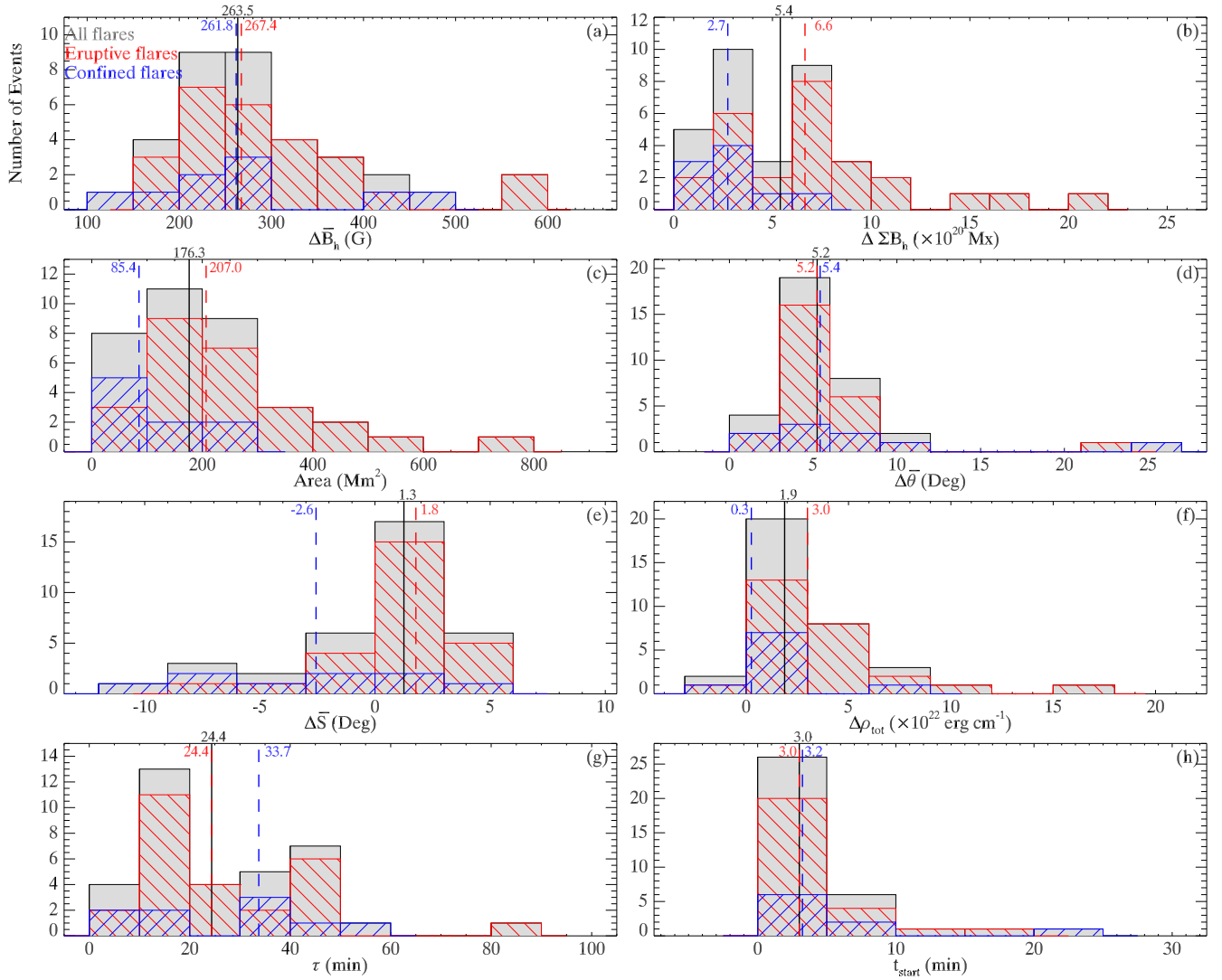


Figure 3. Distributions of the postflare change of the B_h -increase parameters. In each panel, the vertical lines, with the digits above, mark the parameter medians for the corresponding samples (black, red, and blue for all, eruptive, and confined flares, respectively).

$\Delta\bar{B}_h = 220.0 + 357.6e^{-0.36 \times \text{IRS}}$ (reduced chi-square $\chi_r^2 = 0.61$). Given the large uncertainty of $\Delta\bar{B}_h$, it is more appropriate to see the fitting only as a reference. Moreover, the timescale τ of the B_h increase shows a significant correlation with IRS ($cc = 0.71$; Figure 5(b)). These indicate that a smaller initial ribbon separation tends to be accompanied by a B_h increase of larger intensity and shorter timescale.

We also check the correlation between the flare magnitude and the parameters and find an overall weak trend that larger flares are accompanied by a B_h increase of larger intensity and shorter timescale (Figures 5(c)–(d)).

4. Summary and Discussion

In this work, we investigate the photospheric horizontal field increase in 35 major flares using the HMI high-cadence field data and obtain the following results, which may deepen our understanding of the flare-related B_h increase:

1. The B_h increase appears in every case, accompanied by the field inclination increase. This supports the magnetic field rooted in this region becoming more inclined after the flare.

2. The B_h increase is usually initiated near the flare ribbons, showing a step-like change that evolves in a limited region in between the straight parts of the flare ribbons. In particular, its evolution in the early flare phase shows a close spatiotemporal correlation to flare ribbons. Because the ribbons highlight loop footpoints, these suggest that B_h increase is closely related to flare loops evolution.
3. The intensive parameter of the B_h increase (mean B_h) shows no statistical difference in confined and eruptive flares, while the extensive parameters (total B_h and area) tend to be larger in eruptive flares. These suggest that the process leading to B_h increase tends to affect a larger photospheric area during CME-associated flares.
4. The intensity and timescale of the B_h increase are inversely and positively correlated to the IRS, respectively. Because the IRS indicates the height where flare reconnection initiates (see Section 3.2), these suggest that the process leading to B_h increase may start along with the flare reconnection and then propagates downward, resulting in a faster and stronger photospheric effect when the propagating path is shorter (lower reconnection height).

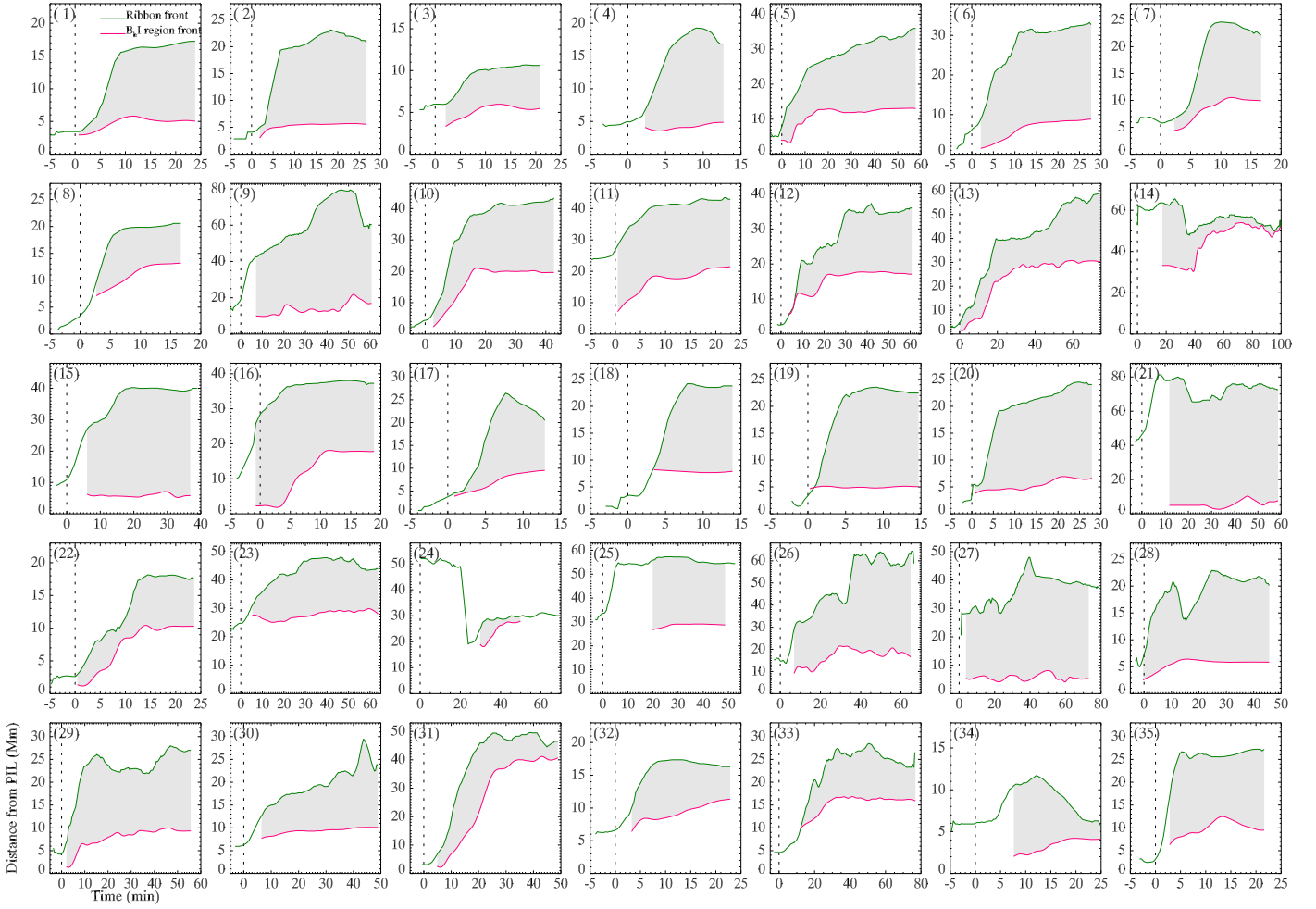


Figure 4. Evolution of the distances from the region’s fronts to the flaring PILs in all cases, with red (green) for the B_h -increase region (flare ribbons). The subcaptions indicate case numbers in Table 1. The vertical lines mark the flare’s start. The shaded regions mark the coexistence duration of the B_h increase and flare ribbons.

The above results altogether support that B_h increase results from the flare reconnection-driven contraction of the flare loops, governed by the induction equation (Barczynski et al. 2019). The first finding (item 1) supports the occurrence of flare-loop contraction, consistent with previous studies (see Section 1). The second further supports a flare-loop-related origin for B_h -increase. The third has a natural interpretation from the standard flare model: The upward motion of CMEs in eruptive flares tends to result in more flare loops that may sweep a wider photospheric area. The fourth is well explained when considering the induction equation: A smaller IRS indicates lower, shorter flare loops formed in the early flare phase, which may relax downward faster and brake sharply with the tension-driven jet, resulting in a larger $\frac{\partial u_z}{\partial z}$, which amplifies the photospheric B_h more quickly and significantly. The higher, longer loops formed later tend to behave oppositely, explaining why the B_h increase only follows the ribbons in the early flare phase. This is analogous to the phenomenon revealed in simulations: B_h increase occurs slower in regions later swept by current ribbons (Barczynski et al. 2019). Note the latter three findings are systematically identified here for the first time. Besides the above results, the identified shear increase is also consistent with the shear transfer process suggested in the 3D flare model.

Our results suggest that B_h increase is consistent with the standard flare model. Although the model is proposed for eruptive flares, the difference in the B_h increase in confined and eruptive flares identified here is not striking (see item 3 above). This might be because even some confined flares may still involve confined flux-rope eruptions. A flare showing observable signatures of a confined eruption of possible flux ropes (e.g., filaments or hot channels) is called a failed eruption (Ji et al. 2003). In that case, the flux rope also rises, leading to the formation of a current sheet below, but fails to propagate out due to strong confinement above (Török & Kliem 2005). The flare thus tends to have similar properties to an eruptive flare (Harra et al. 2016). However, its ribbons may sweep a smaller photospheric area as the flux rope stops ascending earlier, consistent with our findings above (item 3). For the confined flare not involving a flux rope, observations suggest that flare reconnection may occur between multiple magnetic systems, and about one-third of observed confined flares belongs to this category (Li et al. 2019). Considering that around 27% (9/35) of our cases are confined flares, the portion of the category is quite small, which may not significantly affect our statistical results regardless of what their B_h -increase properties are.

The implosion conjecture (Hudson 2000) is often used to explain the B_h increase (see Section 1). Although our results support a reconnection-driven origin for the B_h increase, the

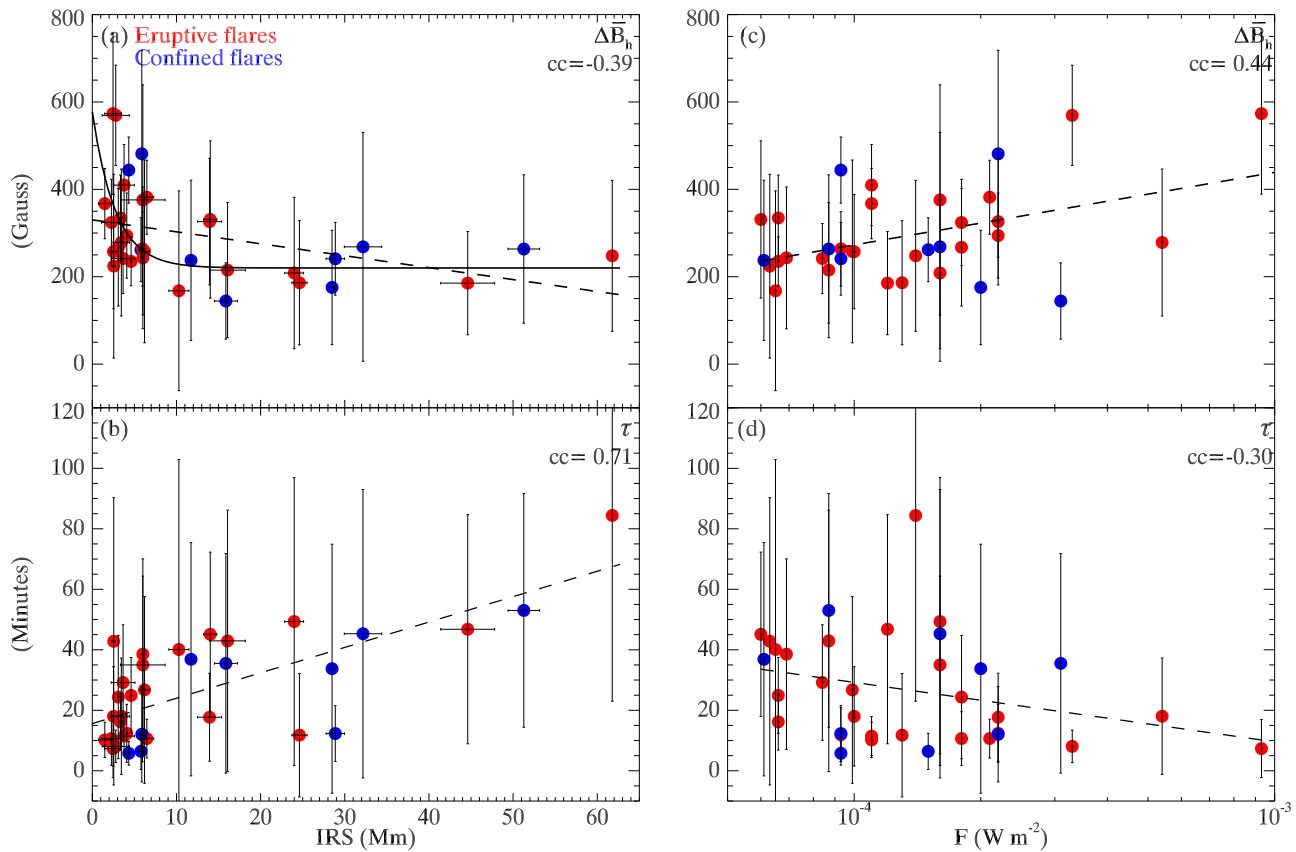


Figure 5. (a)–(b) Scatter plots between two B_h -increase parameters and IRS. The solid curve in (a) represents an exponential fitting. The dashed line represents the linear fitting. “cc” indicates the correlation coefficient. (c)–(d) Scatter plots between the parameters and flare magnitude shown for comparison.

implosion should still be consistent with the process because it is just a restatement of the universal rule of energy conservation. The conservation of momentum during coronal eruptions (Hudson et al. 2012; Fisher et al. 2012) is also used to explain the flare-related B_h increase sometimes (e.g., Barczynski et al. 2019; Wang & Liu 2021). But to our understanding, the CME momentum, and the corresponding downward momentum, is related to the photospheric field change through the Lorentz force change under some approximation, and it only sets a lower limit to the Lorentz force impulse (Fisher et al. 2012). It may not be appropriate to take the momentum conservation as an independent cause of the B_h increase. The identified relatively larger total B_h increase in eruptive flares indeed suggests a larger Lorentz force change in CMEs.

To summarize, our results support that the B_h increase during flares is very likely to be caused by the reconnection-driven contraction of flare loops and is governed by the induction equation.

We thank Haisheng Ji for the helpful discussions. We thank our anonymous referee for constructive comments that significantly improved the manuscript. We acknowledge the SDO, SOHO, and GOES missions for providing quality observations. L.L. is supported by the Guangdong Basic and Applied Basic Research Foundation (2022A1515011548).

ORCID iDs

Lijuan Liu <https://orcid.org/0000-0001-6804-848X>
Zhenjun Zhou <https://orcid.org/0000-0001-7276-3208>

Yuming Wang <https://orcid.org/0000-0002-8887-3919>
Xudong Sun <https://orcid.org/0000-0003-4043-616X>
Guoqiang Wang <https://orcid.org/0000-0002-6618-4928>

References

- Alissandrakis, C. E. 1981, *A&A*, **100**, 197
Aulanier, G. 2016, *NatPh*, **12**, 998
Aulanier, G., Janvier, M., & Schmieder, B. 2012, *A&A*, **543**, A110
Barczynski, K., Aulanier, G., Masson, S., & Wheatland, M. S. 2019, *ApJ*, **877**, 67
Bobra, M. G., Sun, X., Hoeksema, J. T., et al. 2014, *SoPh*, **289**, 3549
Fisher, G. H., Bercik, D. J., Welsch, B. T., & Hudson, H. S. 2012, *SoPh*, **277**, 59
Fletcher, L., & Hudson, H. S. 2008, *ApJ*, **675**, 1645
Gosain, S. 2012, *ApJ*, **749**, 85
Harra, L. K., Schrijver, C. J., Janvier, M., et al. 2016, *SoPh*, **291**, 1761
Hoeksema, J. T., Liu, Y., Hayashi, K., et al. 2014, *SoPh*, **289**, 3483
Hudson, H. S. 2000, *ApJL*, **531**, L75
Hudson, H. S., Fisher, G. H., & Welsch, B. T. 2008, in *ASP Conf. Ser.* 383, *Subsurface and Atmospheric Influences on Solar Activity* (San Francisco, CA: ASP), 221
Hudson, H. S., Fletcher, L., Fisher, G. H., Abbett, W. P., & Russell, A. 2012, *SoPh*, **277**, 77
Janvier, M., Aulanier, G.,ariat, E., & Démoulin, P. 2013, *A&A*, **555**, A77
Ji, H., Huang, G., & Wang, H. 2007, *ApJ*, **660**, 893
Ji, H., Wang, H., Schmahl, E. J., Moon, Y.-J., & Jiang, Y. 2003, *ApJL*, **595**, L135
Kazachenko, M. D., Lynch, B. J., Welsch, B. T., & Sun, X. 2017, *ApJ*, **845**, 49
Kusano, K., Iju, T., Bamba, Y., & Inoue, S. 2020, *Sci*, **369**, 587
Leka, K. D., Barnes, G., & Barnes, G. 2003, *ApJ*, **595**, 1277
Lemen, J. R., Title, A. M., Akin, D. J., et al. 2012, *SoPh*, **275**, 17
Li, T., Liu, L., Hou, Y., & Zhang, J. 2019, *ApJ*, **881**, 151
Li, Y., Jing, J., Fan, Y., & Wang, H. 2011, *ApJL*, **727**, L19
Liu, C., Deng, N., Liu, Y., et al. 2005, *ApJ*, **622**, 722
Liu, C., Deng, N., Liu, R., et al. 2012, *ApJL*, **745**, L4

- Liu, C., Cao, W., Chae, J., et al. 2018, [ApJ](#), 869, 21
- Liu, W., Chen, Q., & Petrosian, V. 2013, [ApJ](#), 767, 168
- Priest, E. R., & Forbes, T. G. 2002, [A&ARv](#), 10, 313
- Shibata, K., & Magara, T. 2011, [LRSP](#), 8, 6
- Simões, P. J. A., Fletcher, L., Hudson, H. S., & Russell, A. J. B. 2013, [ApJ](#), 777, 152
- Sudol, J. J., & Harvey, J. W. 2005, [ApJ](#), 635, 647
- Sun, X. 2013, On the Coordinate System of Space-Weather HMI Active Region Patches (SHARPs): A Technical Note, (arXiv:1309.2392)
- Sun, X., Hoeksema, J. T., Liu, Y., Kazachenko, M., & Chen, R. 2017, [ApJ](#), 839, 67
- Sun, X., Hoeksema, J. T., Liu, Y., et al. 2012, [ApJ](#), 748, 77
- Thalmann, J. K., Su, Y., Temmer, M., & Veronig, A. M. 2015, [ApJL](#), 801, L23
- Toriumi, S., & Wang, H. 2019, [LRSP](#), 16, 3
- Török, T., & Kliem, B. 2005, [ApJL](#), 630, L97
- Wang, H., & Liu, C. 2015, [RAA](#), 15, 145
- Wang, H., Liu, C., Wang, S., et al. 2013, [ApJL](#), 774, L24
- Wang, H., Spirock, T. J., Qiu, J., et al. 2002, [ApJ](#), 576, 497
- Wang, J., Shi, Z., Wang, H., & Lue, Y. 1996, [ApJ](#), 456, 861
- Wang, J., Simões, P. J. A., & Fletcher, L. 2018, [ApJ](#), 859, 25
- Wang, S., Liu, C., Deng, N., & Wang, H. 2014, [ApJL](#), 782, L31
- Wang, S., Liu, C., Liu, R., et al. 2012, [ApJL](#), 745, L17
- Wang, W., & Liu, R. 2021, [A&A](#), 647, A108
- Wheatland, M. S., Melrose, D. B., & Mastrano, A. 2018, [ApJ](#), 864, 159